# Efficient CO_2 Reduction to Formate on $CsPbI_3$ Nanocrystals Wrapped with Reduced Graphene Oxide

Minh Tam Hoang[1,2], Chen Han[3], Zhipeng Ma[3], Xin Mao[1,2], Yang Yang[1,2], Sepideh Sadat Madani[1,2], Paul Shaw[4], Yongchao Yang[3], Lingyi Peng[3], Cui Ying Toe[3,5], Jian Pan[3], Rose Amal[3], Aijun Du[1,2], Tuquabo Tesfamichael[1,2], Zhaojun Han[3] ✉, Hongxia Wang[1,2] ✉

HIGHLIGHTS

- A rational design of metal halide perovskites for achieving efficient CO_2 reduction reaction was demonstrated.

- The stability of $CsPbI_3$ perovskite nanocrystal (NCs) in aqueous electrolyte was improved by compositing with reduced graphene oxide (rGO).

- The $CsPbI_3$/rGO catalyst exhibited > 92% Faradaic efficiency toward formate production with high current density which was associated with the synergistic effects between the $CsPbI_3$ NCs and rGO.

ABSTRACT Transformation of greenhouse gas (CO_2) into valuable chemicals and fuels is a promising route to address the global issues of climate change and the energy crisis. Metal halide perovskite catalysts have shown their potential in promoting CO_2 reduction reaction (CO_2RR), however, their low phase stability has limited their application perspective. Herein, we present a reduced graphene oxide (rGO) wrapped $CsPbI_3$ perovskite nanocrystal (NC) CO_2RR catalyst ($CsPbI_3$/rGO), demonstrating enhanced stability in the aqueous electrolyte. The $CsPbI_3$/rGO catalyst exhibited > 92% Faradaic efficiency toward formate production at a CO_2RR current density of ~ 12.7 mA cm^{-2}. Comprehensive characterizations revealed the superior performance of the $CsPbI_3$/rGO catalyst originated from the synergistic effects between the $CsPbI_3$ NCs and rGO, i.e., rGO stabilized the α-$CsPbI_3$ phase and tuned the charge distribution, thus lowered the energy

barrier for the protonation process and the formation of *HCOO intermediate, which resulted in high CO_2RR selectivity toward formate. This work shows a promising strategy to rationally design robust metal halide perovskites for achieving efficient CO_2RR toward valuable fuels.
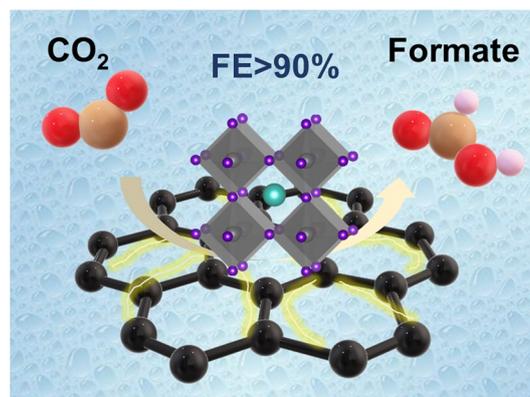
KEYWORDS Perovskite nanocrystal; Electrocatalyst; Inorganic perovskite; CO_2 reduction; Formate production

Minh Tam Hoang, Chen Han, Zhipeng Ma, and Xin Mao equally contributed to this work.

✉ Zhaojun Han, zhaojun.han@unsw.edu.au; Hongxia Wang, hx.wang@qut.edu.au

1   School of Chemistry and Physics, Faculty of Science, Queensland University of Technology, Brisbane, QLD 4001, Australia
2   Centre for Materials Science, Queensland University of Technology, Brisbane, QLD 4001, Australia
3   School of Chemical Engineering, The University of New South Wales, Kensington, NSW 2052, Australia
4   Centre for Organic Photonics & Electronics (COPE), School of Chemistry and Molecular Biosciences, The University of Queensland, Brisbane, QLD 4072, Australia
5   School of Engineering, The University of Newcastle, Callaghan, NSW 2038, Australia

1 Introduction

Metal halide perovskites (MHPs) are recognized as one of the most effective materials for solar-to-electrical energy conversion [1–3]. Recently, the interesting electrical properties of MHPs have inspired the exploration of their applications in catalytic reactions including CO_2 reduction, water splitting, organic synthesis, and dye degradation [4–12]. The versatility of chemical tailoring and ion combination of the MHPs makes them suitable for many different catalytic reactions [13–15]. However, the application of MHPs for electrocatalysis remains challenging due to their low stability, particularly under electrocatalytic conditions [16, 17].

The catalytic property of MHPs was firstly demonstrated in 2016 by Park et al. They used methylammonium lead triiodide (MAPbI$_3$) MHP for solar-driven electrochemical hydrohalic acid splitting for H_2 production, which achieved a Faradaic efficiency (FE) of almost 100% [18], where the MAPbI$_3$ was stabilized by utilizing the precipitation–solubility equilibrium between the perovskite phase and the soluble ionic species in aqueous electrolyte. This opens an appealing chapter of metal halide perovskites for catalytic applications [19]. Especially, in the field of electrochemical reduction of CO_2, the inorganic MHP CsPbBr$_3$ exhibited significant electrocatalytic activity with FE of 32% for CH_4 and 40% for CO [20]. In addition, mixed halides CsPb(Br$_{0.5}$Cl$_{0.5}$)$_3$ MHP catalyst boosted solar-driven electrochemical production of CO from CO_2 with a yield of 875 $\mu mol\ g^{-1}$ and selectivity up to 99% [21], while the MAPbI$_3$ catalyst incorporated in iron-porphyrin derived metal–organic frameworks delivered a high total yield of 1559 $\mu mol\ g^{-1}$ for photocatalytic CO_2 reduction to CO (34%) and CH_4 (66%) [22]. These studies have shown the application potential of MHPs in electrochemical CO_2RR toward valuable fuels. Although there are potential environmental and health risks associated with the use of lead-based MHP catalysts, research of this type of material for CO_2RR is still important fundamentally. Pb-based catalysts such as Pb nanoparticles or Pt$_n$Pb nanocrystals have shown excellent effectivity and selectivity in CO_2RR [23–25], however the study of the potential of Pb-based metal halide perovskites for CO_2 reduction is very limited. Moreover, from economical point of view, the much lower material cost and the ease of scalability of Pb-based MHP materials by solution method also make them very attractive compared to the precious metal-based catalysts for CO_2RR, such as platinum which have been widely studied for CO_2RR application.

Nevertheless, significant research challenges for the development of MHPs CO_2RR catalysts remain [26]. One daunting issue hindering their application is the instability of MHPs in the majority of common CO_2RR electrolytes. MHPs are highly unstable in polar solvents, especially under catalytic reaction conditions where radical species are involved. Hence, low-polarity solvents, such as ethyl acetate, acetonitrile, or toluene were previously used as electrolyte solvent to preserve the phase and optoelectrical properties of MHPs catalysts [4, 11, 27]. However, the catalytic performance of MHPs in these electrolytes is unfavourable due to the low solubility of CO_2 in these low polarity solvents [28]. Therefore, catalyst design strategies based on hybrid MHPs with different materials, i.e., graphene oxide [29], Pt nanoparticles [30], metal–organic frameworks [31, 32], have been used to enhance the stability of the MHPs. For example, the hybrid CsPbBr$_3$ nanocrystals (NCs) with graphitic carbon nitride showed enhanced stability in both acetonitrile/water and ethyl acetate/water solvent systems, while exhibited enhanced photocatalytic CO production rate of 149 $\mu mol\ h^{-1}\ g^{-1}$ [27]. However, the lifetime of MHP-based catalyst is still far from the requirement for a substantial electrolysis system [33]. It is thus critical to resolve the instability of MHPs in the catalytic reaction conditions. In addition, most of the efforts have been devoted into the study of CsPbBr$_3$ catalysts with the primary reduction products of CH_4 and CO; whereas electrochemical CO_2 reduction toward other valuable chemicals has not been demonstrated.

Herein, we demonstrate an inorganic CsPbI$_3$ perovskite NCs wrapped with reduced graphene oxide (rGO) for CO_2RR in aqueous electrolyte, which exhibited increased stability compared with the bare CsPbI$_3$ perovskite NCs. In addition, the CsPbI$_3$/rGO catalyst exhibited outstanding activity (j_{CO2RR} of 12.7 mA cm^{-2}) and selectivity (FE$_{formate}$ of 92%), which is attributed to the accumulated electron density near the active CsPbI$_3$ perovskite structure induced by the rGO wrapping, as evidenced by experimental characterization and density functional theory (DFT) modelling. Together with the unravelled CO_2RR mechanism of CsPbI$_3$/rGO catalyst, this work unleashes the potential of

inorganic MHPs as robust and efficient CO_2RR catalysts for sustainable fuels production.

2 Experimental Section

2.1 Materials

Chemicals including Cs_2CO_3 (99.95%, Sigma Aldrich), Oleic Acid (≥ 99%, Sigma Aldrich), Octadecene (Sigma Aldrich), PbI_2 (99.99%, Sigma Aldrich), $KHCO_3$, Oleylamine (Sigma Aldrich), reduced graphene oxide (Sigma Aldrich), Methyl acetate, Hexane was used as received without further purification.

2.2 Synthesis of Perovskite NCs

The synthesis procedures were carried out following a published method in literature with some modifications [34]. Cs-Oleate was prepared by adding 202.8 mg of Cs_2CO_3 and 10 mL Octadecene (ODE) into a 100 mL three-neck flask. The flask was then degassed and dried under vacuum at 120 °C for 30 min. Subsequently, 0.63 mL of Oleic Acid (OA) was also added into the solution and the system was degassed for another 30 min. After that, the mixture was heated to 160 °C under N_2 gas and stirred until all the Cs_2CO_3 was dissolved to make a clear solution. The Cs-oleate solution is kept at 100 °C under N_2 gas for further use.

In another three-neck flask, 0.3 mg of PbI_2 and 20 mL ODE were loaded. The flask also was degassed and dried under vacuum for 1 h at 120 °C. A mixture of 1.5 mL OA and 1.5 mL Oleylamine (OLA) was added into the flask during this time. After PbI_2 was completely dissolved, the temperature was raised to 170 °C and was kept stirring in N_2 gas for 20 min. At this state, 1.5 mL of as-prepared Cs-Oleate (preheated at 100 °C) was quickly injected into the PbI_2 solution. About 5 s later, the reaction was quenched in an ice bath. After the flask was cooled down to room temperature, 20 mL of methyl acetate was added to precipitate the NCs. The NCs were then collected by centrifugation at 10,000 rpm for 10 min. After that, the supernatant was discarded, and the collected NCs were dispersed in 10 mL of Hexane. The solution then goes through another centrifuging step at 8000 rpm for 5 min. The precipitate is

collected and kept in vacuum for 6 h to remove the residual solvents. The final NCs were dispersed in Hexane for further measurement and applications.

2.3 Catalyst Preparation

The electrodes were prepared by mixing carbon black and catalysts with a mass ratio of 1 and painted on carbon fiber paper.

To specific, the electrode for the H-cell test was prepared through a drop-casting method. Firstly, 5 mg $CsPbI_3$/rGO catalyst was dispersed in 1 mL hexane, and the catalyst ink was then mixed with 5 mg carbon black and ultrasonicated for 10 min. Finally, the obtained catalyst ink was drop-casted onto a carbon fiber paper (Toray Carbon Paper 090) and used as the electrode for the H-cell CO_2 reduction test after drying in a vacuum desiccator for 5 h. For preparing the electrode for flow-cell test, 5 mg $CsPbI_3$/rGO catalyst dispersed in 1 mL hexane, 5 mg Polytetrafluoroethylene (PTFE) powder (diameter of 1 μm) and 5 mg carbon black, then the obtained catalyst ink was sprayed onto a carbon fiber paper (AvCarb GDS2230) coated with PTFE and used as the electrode for flow-cell CO_2 reduction test after drying in a vacuum desiccator for 5 h.

2.4 Electrochemical CO_2 Reduction Experiments

The electrochemical CO_2 reduction experiments in H-cell were conducted in a three-electrode H-Cell reactor filled with CO_2-saturated 0.1 M $KHCO_3$ solution (Sigma Aldrich, 99.7%). The synthesized $CsPbI_3$/rGO electrode was used as the working electrode, while Pt foil and Ag/AgCl electrodes were used as counter and reference electrodes, respectively. The working electrode and counter electrode were separated by a Nafion 117 membrane (Dupont) and connected to Autolab potentiostat (PGSTAT204). Each sample was evaluated for 1.5 h before the gas phase products were collected for analysis using gas chromatography (GC-2010, Shimadzu). The liquid phase products were analyzed by nuclear magnetic resonance (Avance III 600 MHz NMR, Bruker) using a presaturation method for water suppression.

The electrochemical CO_2 reduction experiments in flow cell were conducted in a two-electrode flow-cell reactor with continuously pumped-in 1.0 M $KHCO_3$ solution (Sigma Aldrich, 99.7%) at flow rate of 3 mL min^{-1} in the cathode ($CsPbI_3$/rGO) side with 1.0 M KOH (Sigma Aldrich, 85.0%) in the anode (Ni foam) side. The CO_2 gas continuously flowed through the back side of the cathode at flow rate of 50 mL min^{-1} via a custom-designed gas gate. The working electrode and counter electrode were separated by a Sustainion® anion exchange membranes and connected to Autolab potentiostat (PGSTAT204) equipped with a BOOSTER10A module. The gas phase and liquid phase products were collected for analysis using gas chromatography (GC-2010, Shimadzu) and nuclear magnetic resonance (Avance III 600 MHz NMR, Bruker) using the same method as the above-mentioned for the H-cell CO_2 reduction test. The electrochemical impedance spectroscopy (EIS) was tested in CO_2-saturated 0.1 M $KHCO_3$ aqueous solution under 0 V vs RHE with frequency range of 0.01–10^5 Hz.

2.5 Characterization

Characterization was conducted to reveal the structure, optical and electrical properties of the synthesized materials. UV–visible absorbance spectrum of the samples was measured by a UV–visible spectrometer (Carry 60), and the photoluminescence spectrum was recorded with a Cary Eclipse Fluorescence Spectrophotometer. The TEM images were captured by a JEOL 2100 microscope operated at 200 kV. STEM-EDS was obtained using an EDS detector coupled with JEOL 2100 TEM. A Kratos AXIS Supra photoelectron spectrometer (He I radiation, $h\nu = 21.22$ eV) was used to measure the XPS spectra and the UPS energy state of the materials. The crystal structure of the NCs were measured by X-ray diffraction equipment (Rigaku Smartlab) using a monochromatic CuKα ($\lambda = 0.154$ nm) as a radiation source. Fourier transform infrared (FTIR) spectrum was recorded by a Bruker model Alpha-P FTIR with ATR accessory. Time-resolved photoluminescence (TRPL) was measured by an Edinburgh fluorescence spectrometer at room temperature. The photo-excited source was provided by a laser with exciting wavelength of 474 nm and a pulse of 82.4 ps. *In-situ* and *ex-situ* Raman spectroscopy was performed with a

Renishaw inVia Qontor spectrometer with exciting wavelength of 514 nm.

2.6 DFT Calculation

All the calculations for the optimization of $CsPbI_3$ (001) plane and graphene-decorated $CsPbI_3$ (001) were performed by using the density functional theory (DFT) method as implemented in the Vienna Ab initio Simulation Package (VASP). The Perdew–Burke–Ernzerhof (PBE) function of the generalized gradient approximation (GGA) was used for the calculation of electron exchange–correlation with the projector augmented wave (PAW) method [1–3]. Spin-polarization was also included through the calculations, and the cut-off energy of 500 eV for plain-wave basis sets was adopted. The convergence threshold was set to 10^{-5} eV, and 5×10^{-3} eV $Å^{-1}$ for energy and force, respectively. The weak interaction was treated by DFT + D3 method using an empirical correction in Grimme's scheme [4]. The reaction Gibbs free energy changes (ΔG) for each elementary steps were calculated using the computational hydrogen electrode model shown in the following equation:

$$\Delta G = \Delta E + \Delta ZPE - T\Delta S + \Delta G_U + \Delta G_{pH} \tag{1}$$

where ΔE is obtained directly from DFT calculations, ΔZPE is the change of zero-point energies (ZPE), T is the temperature of 298.15 K, and ΔS is the change in entropy of products and reactants. $\Delta G_U = -eU$, which is the contribution of the electrode potential to ΔG, and $\Delta G_{pH} = -k_BT\ln10 \times pH$.

3 Result and Discussion

3.1 Growth of $CsPbI_3$ on rGO

$CsPbI_3$ NCs were synthesized using a hot-injection synthetic method developed by Protesescu et al. [34]. To synthesize the $CsPbI_3$/rGO composites, rGO was introduced into the PbI_2 precursor solution before the injection of Cs-oleate precursor to initiate the growth of perovskite NCs. Previous studies have shown that perovskite materials have a strong binding affinity to rGO, leading to perovskite crystals readily growing and attaching onto the graphene surface [5, 29, 35]. Transmission electron microscopy (TEM) was used to reveal the structure of the NCs. Figure 1a shows the morphology of reference $CsPbI_3$ NCs which are well

dispersed cubic particles with an average size of ~ 13 nm. The observed lattice spacing of ~ 0.62 nm corresponds to (100) plane of cubic phase $CsPbI_3$ perovskite as revealed in the high-resolution TEM image (inset of Fig. 1a). For the $CsPbI_3$/rGO composite (Fig. 1b), the NCs are distributed on the rGO substrate with a slightly larger size and varying degrees of aggregations, implying that the presence of rGO can induce non uniform nucleation and growth of $CsPbI_3$ NCs. Nevertheless, the $CsPbI_3$ NCs grown on rGO still exhibit crystallinity of cubic phase perovskite. The existence and distribution of $CsPbI_3$ perovskite on the rGO were also confirmed in the energy dispersive X-ray (EDX) mapping, which shows that Cs, Pb and I are well distributed on the rGO substrate (Fig. S1). In addition, the crystallinity of perovskite NCs was determined by X-ray diffraction (XRD). As seen in Fig. 1c, both $CsPbI_3$ NCs and $CsPbI_3$/rGO composite showed similar XRD patterns with characteristic peaks of cubic phase $CsPbI_3$ perovskite (PDF No. 01-080-4039). The $CsPbI_3$ NCs exhibited a preferential orientation at the (100) and (200) planes. In the $CsPbI_3$/rGO composite, besides the peaks attributed to the cubic phase $CsPbI_3$ perovskite, an additional peak at 23.2° was observed, which corresponds to the (002) plane of rGO [36].

Since the surface properties of the nanocrystals catalyst are critical for the electrocatalytic reaction [13, 37], we characterized the chemical composition and chemical state of the synthesized $CsPbI_3$/rGO composite by X-ray photoelectron spectroscopy (XPS). The XPS survey scan clearly identified the C 1s, N 1s, O 1s, Cs 3d, Pb 4f, and I 3d peaks (Fig. S2). Fitting of the C 1s spectra has shown peaks at binding energies of 285.0, 286.2, 286.8 and 289.1 eV, which can be assigned to C–C, C=C, C–O and C=O bonds, respectively [38]. The C 1s features should originate from the surface ligands (oleic acid, oleylamine) used in the NCs synthesis and rGO. High resolution XPS of Cs, Pb and I are shown in Fig. S3. The fitted Cs 3d (725.4 and 739.3 eV), Pb 4f (139.1 and 143.8 eV) and I 3d (619.8 and 631.4 eV) peaks are consistent with the characteristic binding energy of $CsPbI_3$ NCs [39]. Compared to the XPS spectra of $CsPbI_3$, it shows that the introduction of rGO slightly alters the surface property of the $CsPbI_3$ NCs (Fig. S3) with a small XPS peak shift (up to 0.4 eV) in all Cs 3d, Pb 4f and I 3d peaks, implying a change in the distribution of electrons on the surface of $CsPbI_3$. The origin and consequence of this change will be discussed later. The existence of surface ligands of the NCs

was also confirmed by FTIR measurement (Fig. S4). The FTIR spectra show the vibration peaks of the C–C and C–H stretching modes of the CH_2 group and the C=O and O–H characteristic vibrations of the carboxylate ligand. There is a small increase in the intensity of C=O and O–H vibrations in the $CsPbI_3$/rGO composite, which is possibly due to the contribution of rGO. All the above results have confirmed that the cubic phase $CsPbI_3$ NCs have successfully grown on the rGO layers.

Raman spectroscopy is a powerful method to characterize carbon materials [40]. The pristine rGO shows two distinguishable peaks at 1350 (D band) and 1586 (G band) cm^{-1} (Fig. 1d) with the intensity ratio of I_D/I_G ~ 1.16. The G band arises from the C–C stretching in the sp^2-carbon networks and the D band originates from the presence of disorder or defects in the rGO [40, 41]. In the $CsPbI_3$/rGO composite, the two characteristic peaks of D and G bands were also detected, validating the presence of rGO. Interestingly, the band ratio of I_D/I_G is reduced to 1.08 in the $CsPbI_3$/rGO composite. This implies that the loaded $CsPbI_3$ NCs possibly passivate the defects on the surface of rGO.

3.2 Optical Properties and Stability

Perovskite nanocrystals are remarkable in terms of their light emitting properties which is closely related to the crystal structure and electronic properties of the materials [42]. Thus, optical properties of the as-synthesized perovskite NCs were measured to investigate the structural and electronic properties of the materials. As can be seen in Fig. 2a inset, the $CsPbI_3$ NCs solution exhibits strong red emission under UV light (365 nm) excitation. The absorption and photoluminescence characteristics of the as-synthesized $CsPbI_3$ (Fig. 2a) show an absorption onset of ~ 720 nm and an emission peak at 682 nm with full-width-at-half-maximum (FWHM) of 35 nm. The calculated band gap is ~ 1.71 eV (Fig. S5), which is typical for the cubic phase $CsPbI_3$ perovskite [43]. By using a reference dye Rhodamine 6G [44, 45], we determined the photoluminescence quantum yield (PLQY) of the NCs to be ~ 73% (Table S1). In contrast, the $CsPbI_3$/rGO exhibits much lower photoluminescence intensity (Fig. 2a) with a PLQY of 51%. A small red-shift in the absorption onset and PL photoemission peak position (688 nm) are also observed with the composite.
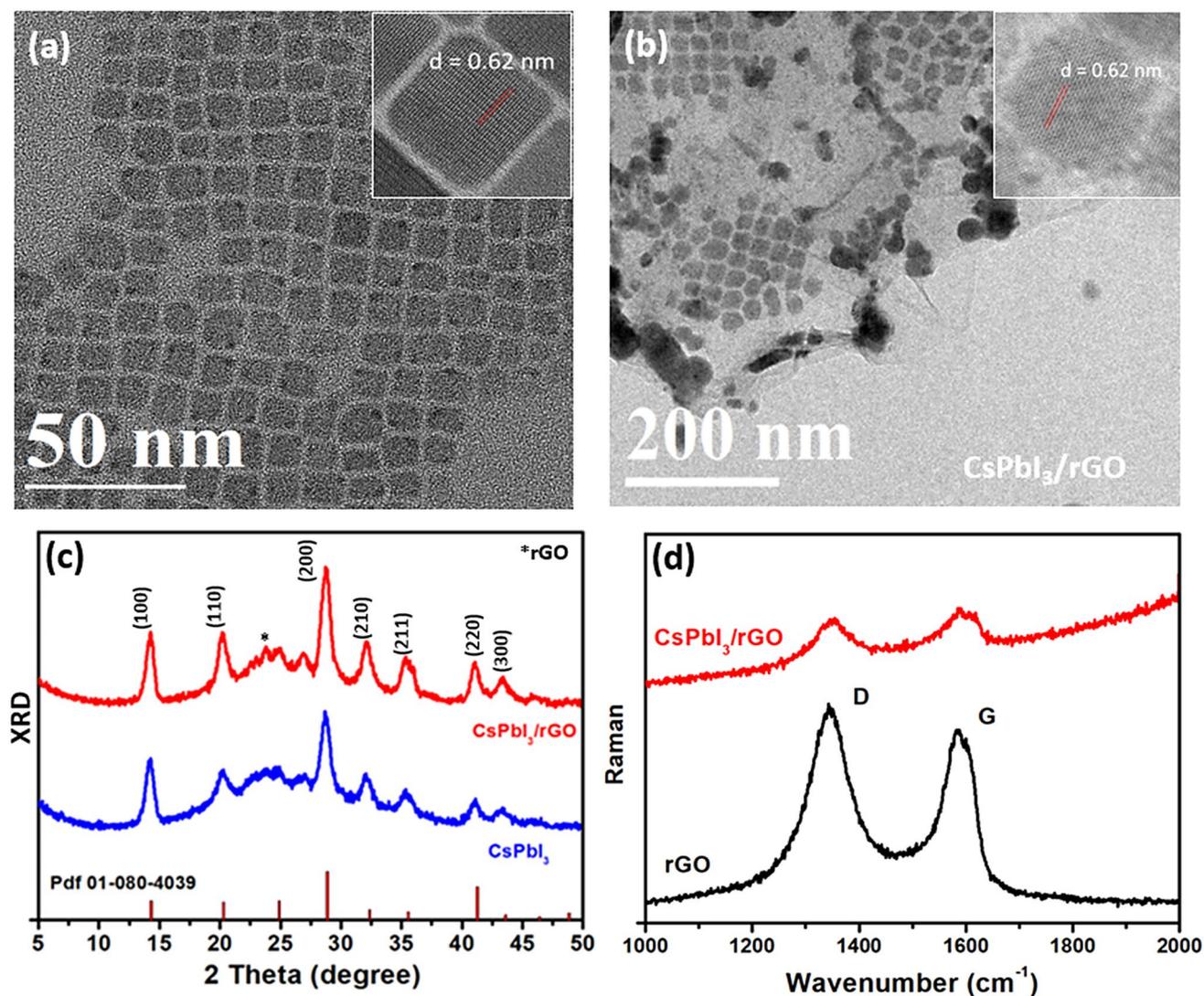
Fig. 1 TEM images reveal the morphology of **a** CsPbI$_3$ NCs and **b** CsPbI$_3$/rGO composite (insets are the high-resolution TEM showing lattice fringe of the CsPbI$_3$ NCs). **c** XRD pattens of CsPbI$_3$ and CsPbI$_3$/rGO composite together with the standard cubic phase CsPbI$_3$ (PDF 01-080-4039). **d** Raman spectra of rGO and CsPbI$_3$/rGO

The red-shift of 6 nm (~ 15.9 meV) could originate from the aggregation of NCs on the rGO sheets as observed in the TEM measurement. The lower PLQY implies that there is significant PL quenching in the material. This is confirmed by the time-resolved PL (TRPL) measurements (Fig. 2b). It shows that the presence of rGO has shortened the PL lifetime of the perovskite NCs. The pristine CsPbI$_3$ NCs exhibit multi-exponential decays with an average lifetime of 62.1 ns, whereas the CsPbI$_3$/rGO composite shows a 17% reduction of the average PL lifetime to 51.5 ns. Detailed calculation of the TRPL data is shown in Table S2. Apparently, addition of rGO has created an efficient charge transfer channel in the

CsPbI$_3$ NCs, which suppresses the radiative recombination of the excited excitons. Measurement of the energy band alignment of CsPbI$_3$ and rGO by ultraviolet photoelectron spectroscopy (UPS) (Fig. S6a) has confirmed the feasibility for charge transfer between the two materials. The CsPbI$_3$ NCs has a valence band energy edge at -5.6 eV (vs vacuum) while rGO has a work function at -5.2 eV, allowing an efficient hole transfer from CsPbI$_3$ to rGO at the interface between the two materials (Fig. S6b).

Stability is a major problem for CsPbI$_3$ NCs. The pristine NCs inks turned from dark brown to a light-yellow with yellow precipitate after 20 days storage in ambient
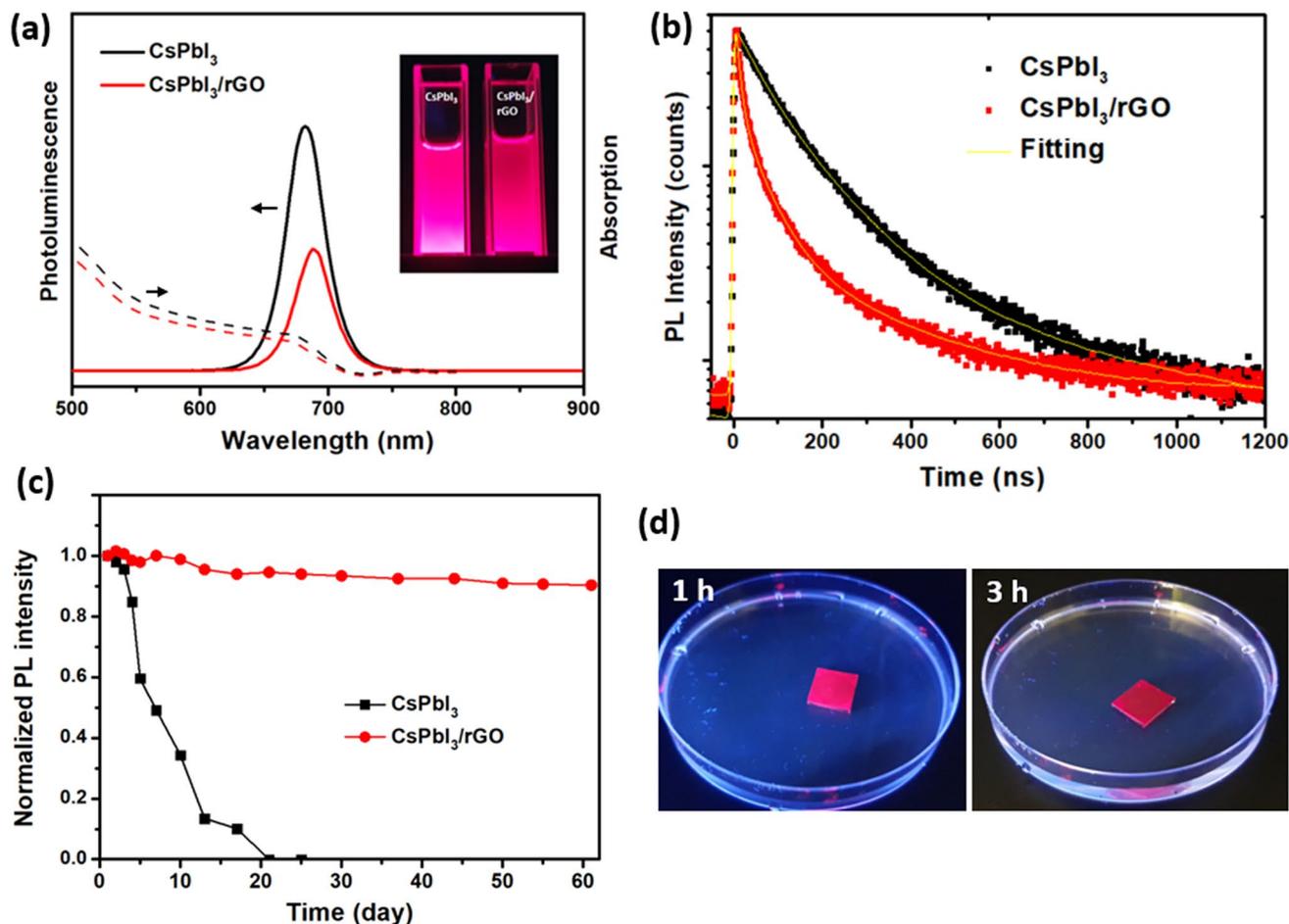
Fig. 2 **a** PL and absorption spectra of CsPbI₃ NCs and CsPBI₃/rGO composite (insets are the photos of two solutions in hexane under UV excitation); **b** TR-PL decay spectra of CsPbI₃ NCs and CsPBI₃/rGO composite; **c** Plots of the change in PL intensity of CsPbI₃ NCs and CsPBI₃/rGO solutions during storage in ambient condition; **d** Photos showing the stability of CsPbI₃/rGO thin film immersed in water for different durations. The film is exhibiting red emission under UV excitation. (Color figure online)

condition (relative humidity 35% ~ 60%) (Fig. S7). This is resulted from the loss of surface ligands, formation of halide vacancy, and eventually the transformation of CsPbI₃ NCs to PbI₂ as reported previously [46, 47]. In contrast, the ink of CsPbI₃/rGO still maintained dark brown colour even after 5 months of storage under the same condition (Fig. S7). The stability of both NCs was further assessed by the PL measurement as shown in Fig. 2c. A dramatical loss in PL intensity was observed in the pristine CsPbI₃ NCs ink during storage, and the PL intensity dropped to zero in 20 days, whereas the CsPbI₃/rGO composite ink still maintained more than 90% of its initial PL intensity after 2 months of storage. The XRD measurement shows

that the CsPbI₃/rGO composite largely retained its cubic phase after 2 months storage, with only a small portion of orthorhombic CsPbI₃ detected (Fig. S8). We further tested the stability of the composite in water. Figure 2d shows the film of CsPbI/rGO composite still exhibited strong light emissions after being immersed in water for 3 h. The water contact angle measurement on the thin film of CsPbI₃ and CsPbI₃/rGO shows that the CsPbI₃/rGO surface is more hydrophobic with a larger contact angle of 81° comparing to CsPbI₃ film which shows a contact angle of approximate 73° (Fig. S9). Clearly, the rGO sheets provide significant protection to the CsPbI₃ against aqueous environment.

3.3 Catalytic CO_2 Reduction Performance

To explore the CO_2RR performance of the $CsPbI_3$/rGO, the CO_2RR experiments over $CsPbI_3$ and $CsPbI_3$/rGO were performed in a typical electrochemical H-cell configuration. The CO_2RR experiments were conducted at different applied potentials ranging from -1.05 to -1.45 V vs reversible hydrogen electrode (RHE). The FE toward CO_2 reduction products is shown in Fig. 3a. It shows that the $CsPbI_3$/rGO catalysts has a higher FE_{CO2RR} under a more negative potential. The FE reaches to more than 90% at -1.45 V vs RHE. Moreover, the $CsPbI_3$/rGO catalysts exhibit a higher selectivity towards formate compared with that of the pristine $CsPbI_3$ catalyst. It should be noted that formate is considered a promising hydrogen energy carrier because of its high volumetric hydrogen storage capacity, low toxicity and low flammability, thus efficient production of formate is desirable in practice [48]. A higher content of H_2 was observed with the pristine $CsPbI_3$ catalyst, which suggests that the interaction between the rGO and the $CsPbI_3$ NCs suppresses the HER process. The gas phase products (i.e., CO and H_2) were quantified by gas chromatography (GC) according to a calibration curve (Fig. S10). The excellent R^2 value ($R^2 > 0.998$) of the calibrate curve ensures the accuracy of the experimental results. The total current density and partial current density of formate are shown in Fig. 3b. The $CsPbI_3$/rGO catalyst exhibits a total current density of 12.7 mA cm^{-2}, in which the formate partial current density accounts for 11.7 mA cm^{-2}. The electrochemical impedance spectroscopy (EIS) of the samples (Fig. S11) were measured to investigate the charge transfer resistance (R_{ct}) of the catalysts in the presence of the CO_2 saturated 0.1 M $KHCO_3$ aqueous solution. The Nyquist plot of EIS was fitted according to the equivalent circuit shown in Inset of Fig. S11. Detail of the fitting results of the EIS spectrum is shown in Table S3. The much lower Rct of the $CsPbI_3$/rGO composite indicates that the introduction of rGO into $CsPbI_3$ has significant benefit for the electrochemical reaction of CO_2RR.

The CO_2RR performance of the $CsPbI_3$/rGO catalyst was further evaluated in a 2-electrode flow-cell system. We achieved ~ 81.0 mA partial current toward CO_2RR products over a 3 cm^2 electrode. This is more than twofold of that in the H-cell system (Fig. S12). The CO_2RR performance of the rGO was tested under the same condition (Fig. S13). However, no CO_2RR product was detected with the bare rGO. Instead, H_2 was the main product with FE ~ 100%. This implies that $CsPbI_3$ is the main active material for the CO_2 reduction in the composite.

We further tested the long-time stability of the catalysts at -1.45 V_{RHE} for 10.5 h continuously. As shown in Fig. 3c, the $CsPbI_3$ alone showed a significant deterioration on the selectivity to formate, with an $FE_{formate}$ of only 52.5% at the end of test. In contrast, the $CsPbI_3$/rGO maintained a $FE_{formate}$ of 76.4% after 10.5 h continuous stability test. This confirms the improved CO_2RR stability of the $CsPbI_3$/rGO catalyst compared with bare $CsPbI_3$. Moreover, the performance of our $CsPbI_3$/rGO catalyst is competitive among other perovskite-based and metal-based catalysts for CO_2 reduction reported in the recent literature such as sulfide-derived Pb or SnO_2 porous nanowires catalyst (Table S4) [49, 50].

To understand this phenomenon, we have analysed the morphology and composition of the fresh and the spent samples. As shown in Fig. 4a, the $CsPbI_3$ without rGO appear in the form of nanoparticles with well-defined crystalline structure dispersed in a carbon matrix. After the first cycle of EC CO_2RR reaction under -1.45 V_{RHE}, the NCs of $CsPbI_3$ without rGO transformed to Pb aggregations (Fig. 4b), as evidenced by the TEM EDX mapping (Fig. 4c). In case of $CsPbI_3$ with rGO, the $CsPbI_3$/rGO catalyst also exhibit the morphology of well-crystalline particles dispersed in a carbon matrix (Fig. 4d), but this morphology remained intact after the same EC CO_2RR condition (Fig. 4e). From the EDS measurement (Fig. 4f), it can be seen that the chemical composition of $CsPbI_3$ NCs in the $CsPbI_3$/rGO was well maintained. The obtained atomic percentages of C, Cs, Pb and I were 98.4%, 0.34%, 0.34% and 0.92%, respectively, corresponding to a Cs/Pb/I ratio of approximately 1/1/2.7, which is close to that of pristine $CsPbI_3$ perovskite phase. After the long-time stability test, despite of the emergence of nanoparticles, the $CsPbI_3$/rGO still preserved the original crystal phase and chemical compounds (Fig. S14), as opposed to the pristine $CsPbI_3$ catalyst which completely changed to Pb particles (Fig. S15). It is noted that the aggregation of $CsPbI_3$ NCs in the $CsPbI_3$/rGO composite led to the formation of nanorods after the long reaction time, which is expected to reduce the surface area of the catalyst and adversely affect the overall electrocatalytic performance.

The structural stability of the samples was further investigated by *in-situ* Raman spectroscopy, which is a powerful method to monitor phase transformation of materials. The
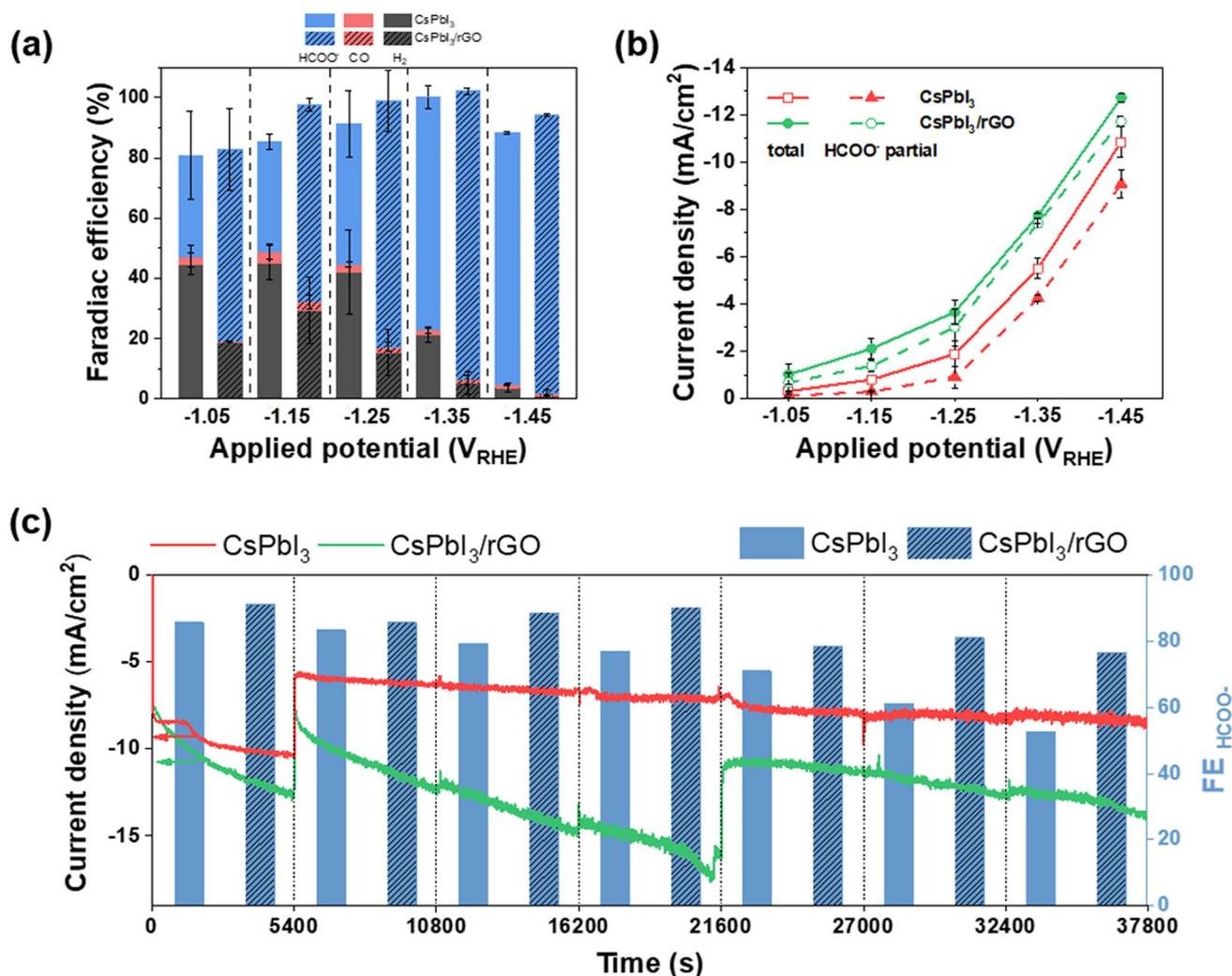
Fig. 3 Electrochemical CO_2 reduction performance of $CsPbI_3$ and $CsPbI_3/rGO$ in CO_2-saturated 0.1 M $KHCO_3$. **a** FE of main products under different applied potentials. **b** Total CO_2RR current density (solid symbols) and partial current density toward formate (dash symbols) under different applied potentials. **c** I–t curves and $FE_{formate}$ in stability test under -1.45 V_{RHE}

pristine $CsPbI_3$ (α-$CsPbI_3$) exhibited an indiscernible Raman peak (Fig. 5a), which is consistent with the previous study that α-$CsPbI_3$ only shows Raman features at a low frequency region [51]. After being aged in the ambient condition, an obvious vibration mode appeared at 108 cm^{-1}, which matches the characteristic fingerprint of δ-$CsPbI_3$, implying that the perovskite undergoes a phase transformation from α-$CsPbI_3$ phase to δ-$CsPbI_3$ phase [51]. The in-situ Raman spectroscopy was used to track phase transition during the EC reaction of $CsPbI_3/rGO$ catalyst. As shown in Fig. 5b, there is no change in the Raman spectra of the $CsPbI_3/rGO$ catalyst under -1.45 V_{RHE} EC CO_2RR conditions in the

1200 s testing period, indicating that the phase transformation to δ-$CsPbI_3$ did not occur and the $CsPbI_3$ in $CsPbI_3/rGO$ remained in the α phase.

We carried out density functional theory (DFT) calculations of binding energy of rGO with α- and δ-$CsPbI_3$ to understand the improved stability of $CsPbI_3/rGO$. As shown in Fig. 5c, d, the binding energy of rGO with α-$CsPbI_3$ (black phase) is -1.533 eV, which is significantly lower than that of rGO with δ-$CsPbI_3$ (yellow phase) (-0.894 eV), suggesting that the $CsPbI_3$ NCs formed on rGO sheets preferably maintains the α-$CsPbI_3$ phase thermodynamically. This also explains the enhanced stability of the α-$CsPbI_3$ in the $CsPbI_3/rGO$
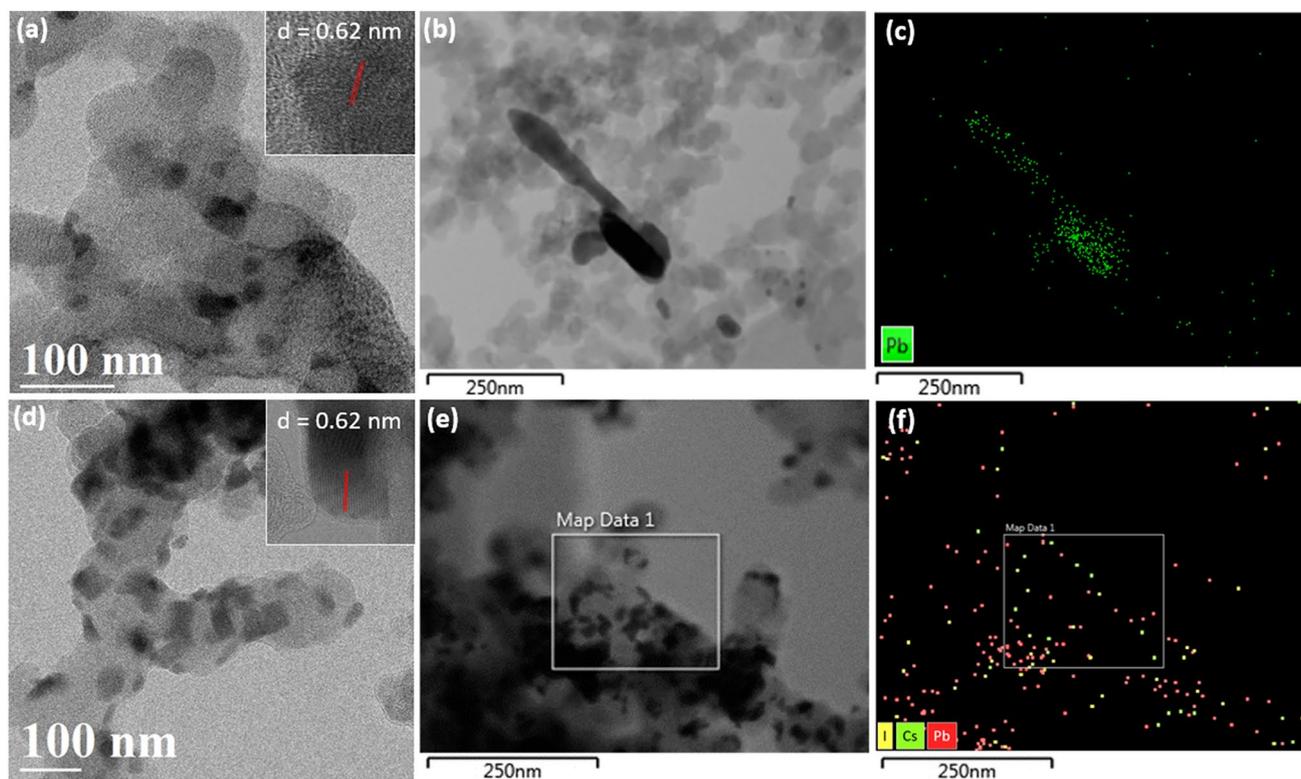
Fig. 4 **a** TEM images of fresh electrodes CsPbI₃; **b** TEM image of CsPbI₃ after one EC CO₂RR run under − 1.45 V_{RHE} and **c** the corresponding EDS elemental mapping image; **d** TEM image of fresh CsPbI₃/rGO electrode; **e** TEM of CsPbI₃/rGO electrode after one EC CO₂RR run under − 1.45 V_{RHE} and **f** the corresponding EDS elemental mapping of composite for Cs (green), Pb (red), I (yellow) elements. (Color figure online)

composite compared to the pristine CsPbI₃ NCs. In addition, comparing the XPS spectra of fresh CsPbI₃ and CsPbI₃/rGO electrodes (Figs. 5e and S16), we have observed a distinct shift toward lower-binding energy in the XPS spectra of Pb 4f, Cs 3d and I 3d of CsPbI₃/rGO. This indicates an increased electron density in the CsPbI₃ material in the presence of rGO. The observation agrees well with the DFT calculation results (Fig. 5f), which show electron transfer between α-CsPbI₃ and rGO, and the electron tends to accumulate around the α-CsPbI₃. The unique charge distribution in CsPbI₃/rGO material plays an important role in the EC CO₂RR performance of the material as discussed below.

3.4 Reaction Pathway

The above results show that the integration of rGO to CsPbI₃ significantly improves the performance, selectivity, and stability of α-CsPbI₃ phase in EC CO₂ reduction. To understand the catalysis mechanism, we calculated the activation energy

of adsorbed species formed in the CO₂ reduction reaction on CsPbI₃ (100) facet with and without rGO, since this is the dominant phase in our material as shown in the XRD (Fig. 1c). Previous theoretical investigations have suggested that Cs cannot be the active site because Cs–C bonding is less favoured than Cs–O bonding [20]. In contrast, the Pb–C bonding is favourable to form. Therefore, Pb is selected as the active site in the DFT calculations. The activation energy of adsorbed species on Pb site was calculated on models of α-CsPbI₃ with and without rGO supported as illustrated in Fig. 6a, b. The resulting free-energy diagrams are shown in Fig. 6c, d, which include two possible pathways for CO₂ reduction, i.e., (i) reduction of CO₂ to the COOH intermediate toward CO and (ii) reduction of CO₂ to the *HCOO intermediate toward HCOOH. The formation of *HCOO intermediate is thermodynamically favourable according to the simulations. This is consistent with the experimental result of high selectivity toward HCOO⁻ product rather than CO product. Interestingly, when CsPbI₃ is anchored on rGO, the activation
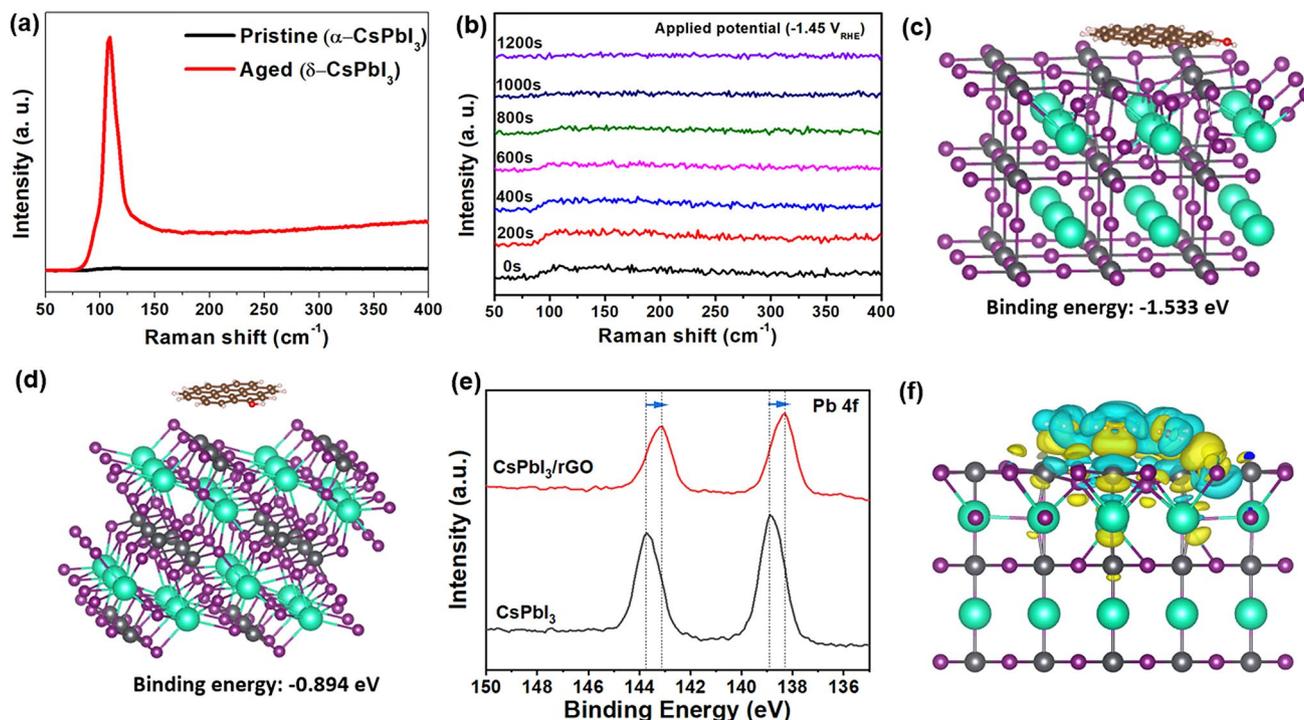
Fig. 5 **a** Raman spectra of pristine CsPbI$_3$ (black) and aged CsPbI$_3$ (red); **b** *In-situ* Raman spectra of CsPbI$_3$/rGO under EC CO$_2$RR conditions with applied potential of -1.45 V_{RHE}; The DFT models of α-CsPbI$_3$ **c** and δ-CsPbI$_3$ **d** with rGO supported and the corresponding calculated binding energy. **e** XPS Pb 4f spectra of fresh CsPbI$_3$ and CsPbI$_3$/rGO electrodes. **g** Electron transfer between α-CsPbI$_3$ and rGO from DFT calculations, where yellow area means charge accumulation, and cyan area means charge depletion. (Color figure online)

energy barrier for *HCOO intermediate formation is reduced from 0.92 to 0.68 eV. It means the CsPbI$_3$/rGO composite can further facilitate the reaction toward the formate production. This is attributed to the electron accumulation formed around Pb atoms in the presence of rGO (Fig. 5f), which strengthens the Pb–C bonding and the adsorption of *H species, followed by the acceleration of the protonation of CO$_2$ for formate formation. It should be noted that the HER is not preferred in both material systems due to the high energy barrier according to our DFT simulation (Fig. S17).

Additionally, we have observed the formation of Pb metal in the spent CsPbI$_3$ catalyst (Fig. 4b). It suggests that the CsPbI$_3$ particles slowly lost Pb atoms during the CO$_2$ reduction reaction. Therefore, a model of CsPbI$_3$ with Pb vacancy was also built to simulate the CO$_2$ reduction reactions. The calculation shows that with Pb vacancy in the CsPbI$_3$ crystal, the energy barrier for *HCOO intermediate formation increases to 1.31 eV (Fig. S18). This explains the decrease of formate selectivity during the long-term stability test in CsPbI$_3$ catalyst. Our results have demonstrated an effective strategy to prevent the phase degradation or Pb defect

formation in CsPbI$_3$, which is critical for maintaining the superior CO$_2$RR performance and formate selectivity.

4 Conclusion

In summary, we have devised an efficient CsPbI$_3$/rGO composite catalyst for CO$_2$RR in aqueous electrolyte. Compared to the pristine CsPbI$_3$ NCs, the α-CsPbI$_3$ perovskite structural degradation in CsPbI$_3$/rGO composite is thermodynamically mitigated, hindering the formation of less-active Pb defects or even Pb particles. Furthermore, by redistributing electrons near the CsPbI$_3$/rGO interface, the rGO lowers the energy barrier for the formation of *HCOO intermediates and protonation process in the CsPbI$_3$/rGO catalyst, thus promoting the CO$_2$RR pathway toward formate product with a high selectivity ($>90\%$ FE$_{formate}$) at applied voltage of -1.45 V vs RHE. The study has revealed the perspective application of metal halide perovskite material in electrochemical CO$_2$RR while paves the way for the development of selective, stable, and active new catalysts.
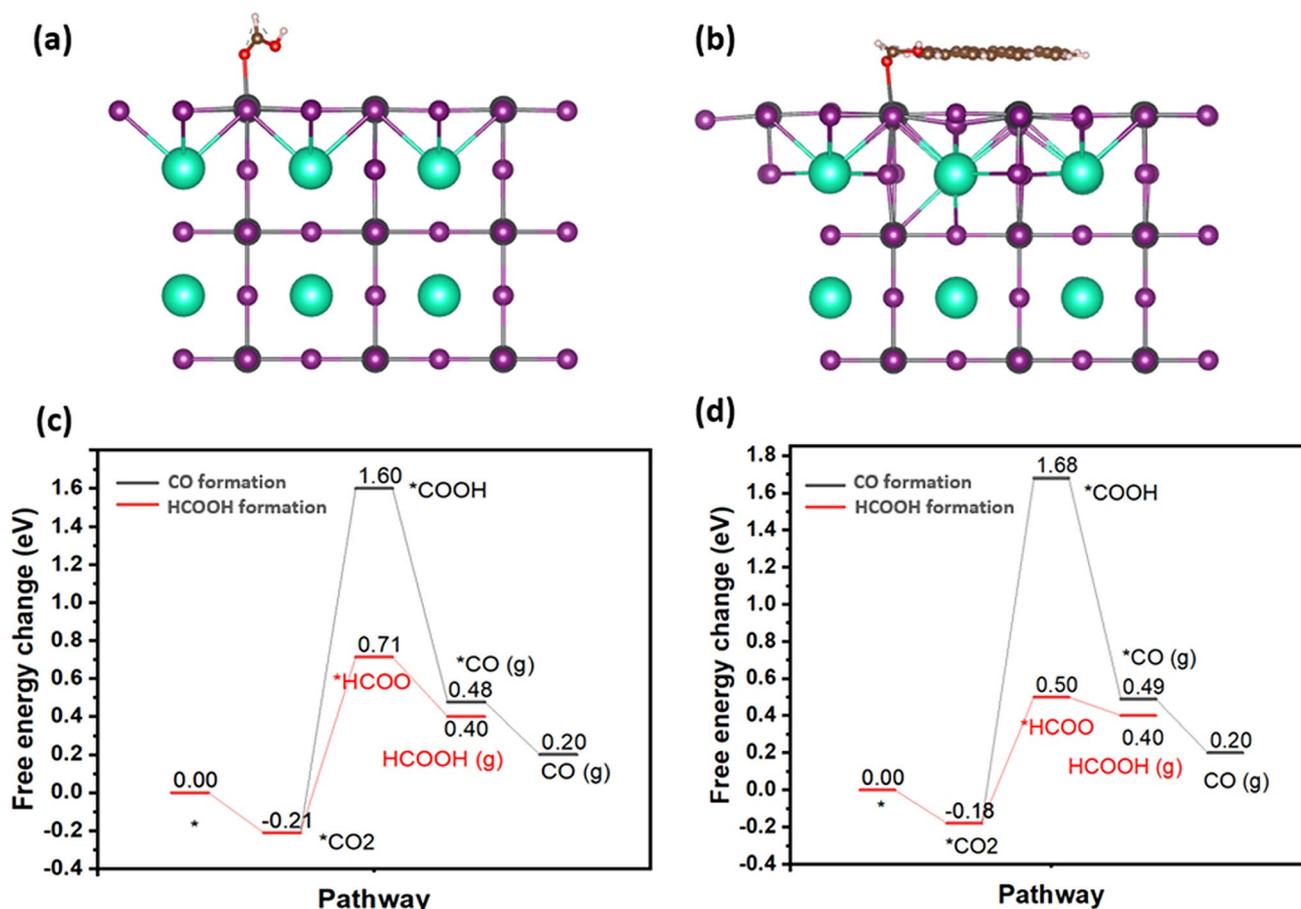
Fig. 6 Models of **a** CsPbI$_3$ and **b** CsPbI$_3$/rGO composite with HCOOH species in the DFT calculations; **c, d** Free-energy diagrams showing the CO and HCOOH formation pathways in the CO$_2$ reduction reaction when **c** CsPbI$_3$ and **d** CsPbI$_3$/rGO catalyst were used

Declarations

Conflict of interest The authors declare no interest conflict. They have no known competing financial interests or personal relationships that could have appeared to influence the work reported in this paper.

References

1. NREL, *Best Research-Cell Efficiencies*, https://www.nrel.gov/pv/assets/pdfs/best-research-cell-efficiencies.20190802.pdf

2. J.J. Yoo, G. Seo, M.R. Chua, T.G. Park, Y. Lu et al., Efficient perovskite solar cells via improved carrier management. Nature **590**, 587–593 (2021). https://doi.org/10.1038/s41586-021-03285-w

3. J. Jeong, M. Kim, J. Seo, H. Lu, P. Ahlawat et al., Pseudo-halide anion engineering for α-FAPbI$_3$ perovskite solar cells. Nature **592**, 381–385 (2021). https://doi.org/10.1038/s41586-021-03406-5

4. J. Hou, S. Cao, Y. Wu, Z. Gao, F. Liang et al., Inorganic colloidal perovskite quantum dots for robust solar CO$_2$ reduction. Eur. J. Chem. **23**, 9481–9485 (2017). https://doi.org/10.1002/chem.201702237

5. Y. Wu, P. Wang, X. Zhu, Q. Zhang, Z. Wang et al., Composite of CH$_3$NH$_3$PbI$_3$ with reduced graphene oxide as a highly efficient and stable visible-light photocatalyst for hydrogen evolution in aqueous HI solution. Adv. Mater. **30**, 1704342 (2018). https://doi.org/10.1002/adma.201704342

6. S. Mollick, T.N. Mandal, A. Jana, S. Fajal, A.V. Desai et al., Ultrastable luminescent hybrid bromide perovskite@ mof nanocomposites for the degradation of organic pollutants in water. ACS Appl. Nano Mater. **2**, 1333–1340 (2019). https://doi.org/10.1021/acsanm.8b02214

7. M. Méndez-Galván, B. Alcántar-Vázquez, G. Diaz, I.A. Ibarra, H.A. Lara-García, Metal halide perovskites as an emergent catalyst for CO$_2$ photoreduction: a minireview. React. Chem. Eng. **6**, 828–838 (2021). https://doi.org/10.1039/D1RE00039J

8. X. Zhu, Y. Lin, J. San Martin, Y. Sun, D. Zhu et al., Lead halide perovskites for photocatalytic organic synthesis. Nat. Commun. **10**, 2843 (2019). https://doi.org/10.1038/s41467-019-10634-x

9. H. Huang, H. Yuan, K.P. Janssen, G. Solís-Fernández, Y. Wang et al., Efficient and selective photocatalytic oxidation of benzylic alcohols with hybrid organic–inorganic perovskite materials. ACS Energy Lett. **3**, 755–759 (2018). https://doi.org/10.1021/acsenergylett.8b00131

10. X. Zhu, Y. Lin, Y. Sun, M.C. Beard, Y. Yan, Lead-halide perovskites for photocatalytic α-alkylation of aldehydes. J. Am. Chem. Soc. **141**, 733–738 (2019). https://doi.org/10.1021/jacs.8b08720

11. K. Chen, X. Deng, G. Dodekatos, H. Tüysüz, Photocatalytic polymerization of 3,4-ethylenedioxythiophene over cesium lead iodide perovskite quantum dots. J. Am. Chem. Soc. **139**, 12267–12273 (2017). https://doi.org/10.1021/jacs.7b06413

12. Y. Wu, Q. Wu, Q. Zhang, Z. Lou, K. Liu et al., An organometal halide perovskite supported Pt single-atom photocatalyst for H$_2$ evolution. Energy Environ. Sci. **15**, 1271–1281 (2022). https://doi.org/10.1039/D1EE03679C

13. J. Hwang, R.R. Rao, L. Giordano, Y. Katayama, Y. Yu et al., Perovskites in catalysis and electrocatalysis. Science **358**, 751–756 (2017). https://doi.org/10.1126/science.aam7092

14. X. Hou, J. Ren, F. Li, C. Ma, X. Zhang et al., Research progress of perovskite materials as catalysts, in I*OP Conference Series: Earth and Environmental Science* (2019), p. 032020.

15. K.P. Kuhl, T. Hatsukade, E.R. Cave, D.N. Abram, J. Kibsgaard et al., Electrocatalytic conversion of carbon dioxide to methane and methanol on transition metal surfaces. J. Am. Chem. Soc. **136**, 14107–14113 (2014). https://doi.org/10.1021/ja505791r

16. V. Adinolfi, W. Peng, G. Walters, O.M. Bakr, E.H. Sargent, The electrical and optical properties of organometal halide perovskites relevant to optoelectronic performance. Adv. Mater. **30**, 1700764 (2018). https://doi.org/10.1002/adma.201700764

17. W. Xiang, S.F. Liu, W. Tress, A review on the stability of inorganic metal halide perovskites: challenges and opportunities for stable solar cells. Energy Environ. Sci. **14**, 2090–2113 (2021). https://doi.org/10.1039/D1EE00157D

18. S. Park, W.J. Chang, C.W. Lee, S. Park, H.-Y. Ahn et al., Photocatalytic hydrogen generation from hydriodic acid using methylammonium lead iodide in dynamic equilibrium with aqueous solution. Nat. Energy **2**, 16185 (2017). https://doi.org/10.1038/nenergy.2016.185

19. J. Luo, W. Zhang, H. Yang, Q. Fan, F. Xiong et al., Halide perovskite composites for photocatalysis: a mini review. EcoMat **3**, e12079 (2021). https://doi.org/10.1002/eom2.12079

20. K. Chen, K. Qi, T. Zhou, T. Yang, Y. Zhang et al., Water-dispersible CsPbBr$_3$ perovskite nanocrystals with ultra-stability and its application in electrochemical CO$_2$ reduction. Nano-Micro Lett. **13**, 172 (2021). https://doi.org/10.1007/s40820-021-00690-8

21. S.-H. Guo, J. Zhou, X. Zhao, C.-Y. Sun, S.-Q. You et al., Enhanced CO$_2$ photoreduction via tuning halides in perovskites. J. Catal. **369**, 201–208 (2019). https://doi.org/10.1016/j.jcat.2018.11.004

22. L.Y. Wu, Y.F. Mu, X.X. Guo, W. Zhang, Z.M. Zhang et al., Encapsulating perovskite quantum dots in iron-based metal–organic frameworks (MOFs) for efficient photocatalytic CO$_2$ reduction. Angew. Chem. Int. Ed. **58**, 9491–9495 (2019). https://doi.org/10.1002/anie.201904537

23. C.X. Zhao, Y.F. Bu, W. Gao, Q. Jiang, CO$_2$ reduction mechanism on the Pb(111) surface: effect of solvent and cations. J. Phys. Chem. C **121**, 19767–19773 (2017). https://doi.org/10.1021/acs.jpcc.7b04375

24. J. García, C. Jiménez, F. Martínez, R. Camarillo, J. Rincón, Electrochemical reduction of CO$_2$ using Pb catalysts synthesized in supercritical medium. J. Catal. **367**, 72–80 (2018). https://doi.org/10.1016/j.jcat.2018.08.017

25. X. Wu, Y. Jiang, Y. Yan, X. Li, S. Luo et al., Tuning surface structure of Pd$_3$Pb/PtnPb nanocrystals for boosting the methanol oxidation reaction. Adv. Sci. **6**, 1902249 (2019). https://doi.org/10.1002/advs.201902249

26. E. Gong, S. Ali, C.B. Hiragond, H.S. Kim, N.S. Powar et al., Solar fuels: research and development strategies to accelerate photocatalytic CO$_2$ conversion into hydrocarbon fuels.

Energy Environ. Sci. **15**, 880–937 (2022). https://doi.org/10.1039/D1EE02714J

27. M. Ou, W. Tu, S. Yin, W. Xing, S. Wu et al., Amino-assisted anchoring of CsPbBr$_3$ perovskite quantum dots on porous g-$_C$3$_N$4 for enhanced photocatalytic CO$_2$ reduction. Angew. Chem. Int. Ed. **57**, 13570–13574 (2018). https://doi.org/10.1002/anie.201808930

28. M.B. Miller, D.-L. Chen, D.R. Luebke, J.K. Johnson, R.M. Enick, Critical assessment of CO2 solubility in volatile solvents at 298.15 K. J. Chem. Eng. Data **56**, 1565–1572 (2011). https://doi.org/10.1021/je101161d

29. Y.-F. Xu, M.-Z. Yang, B.-X. Chen, X.-D. Wang, H.-Y. Chen et al., A CsPbBr$_3$ perovskite quantum dot/graphene oxide composite for photocatalytic CO$_2$ reduction. J. Am. Chem. Soc. **139**, 5660–5663 (2017). https://doi.org/10.1021/jacs.7b00489

30. Y.-X. Chen, Y.-F. Xu, X.-D. Wang, H.-Y. Chen, D.-B. Kuang, Solvent selection and Pt decoration towards enhanced photocatalytic CO$_2$ reduction over CsPbBr$_3$ perovskite single crystals. Sustain. Energy Fuels **4**, 2249–2255 (2020). https://doi.org/10.1039/C9SE01218D

31. Z.-C. Kong, J.-F. Liao, Y.-J. Dong, Y.-F. Xu, H.-Y. Chen et al., Core@ Shell CsPbBr$_3$ @ Zeolitic imidazolate framework nanocomposite for efficient photocatalytic CO$_2$ reduction. ACS Energy Lett. **3**, 2656–2662 (2018). https://doi.org/10.1021/acsenergylett.8b01658

32. R. Cheng, E. Debroye, J. Hofkens, M.B. Roeffaers, Efficient photocatalytic CO$_2$ reduction with MIL-100 (Fe)-CsPbBr$_3$ composites. Catalysts **10**, 1352 (2020). https://doi.org/10.3390/catal10111352

33. T. Burdyny, W.A. Smith, CO$_2$ reduction on gas-diffusion electrodes and why catalytic performance must be assessed at commercially-relevant conditions. Energy Environ. Sci. **12**, 1442–1453 (2019). https://doi.org/10.1039/C8EE03134G

34. L. Protesescu, S. Yakunin, M.I. Bodnarchuk, F. Krieg, R. Caputo et al., Nanocrystals of cesium lead halide perovskites (CsPbX3, X = Cl, Br, and I): novel optoelectronic materials showing bright emission with wide color gamut. Nano Lett. **15**, 3692–3696 (2015). https://doi.org/10.1021/nl5048779

35. Q. Zhang, H. Nan, Y. Zhou, Y. Gu, M. Tai et al., In situ growth of α-CsPbI$_3$ perovskite nanocrystals on the surface of reduced graphene oxide with enhanced stability and carrier transport quality. J. Mater. Chem. C **7**, 6795–6804 (2019). https://doi.org/10.1039/C9TC01012B

36. L. Stobinski, B. Lesiak, A. Malolepszy, M. Mazurkiewicz, B. Mierzwa et al., Graphene oxide and reduced graphene oxide studied by the XRD, TEM and electron spectroscopy methods. J. Electron Spectrosc. Relat. Phenom. **195**, 145–154 (2014). https://doi.org/10.1016/j.elspec.2014.07.003

37. D. Raciti, C. Wang, Recent advances in CO$_2$ reduction electrocatalysis on copper. ACS Energy Lett. **3**, 1545–1556 (2018). https://doi.org/10.1021/acsenergylett.8b00553

38. S. Li, Y. Li, K. Liu, M. Chen, W. Peng et al., Laser fabricated carbon quantum dots in anti-solvent for highly efficient carbon-based perovskite solar cells. J. Colloid Interface Sci. **600**, 691–700 (2021). https://doi.org/10.1016/j.jcis.2021.05.034

39. X. Li, Y. Wu, S. Zhang, B. Cai, Y. Gu et al., CsPbX$_3$ quantum dots for lighting and displays: room-temperature synthesis, photoluminescence superiorities, underlying origins and white light-emitting diodes. Adv. Funct. Mater. **26**, 2435–2445 (2016). https://doi.org/10.1002/adfm.201600109

40. E.I. Bîru, H. Iovu, Graphene nanocomposites studied by Raman spectroscopy. J. Raman Spectrosc. **179** (2018). https://doi.org/10.5772/intechopen.73487

41. A. Kaniyoor, S. Ramaprabhu, A Raman spectroscopic investigation of graphite oxide derived graphene. AIP Adv. **2**, 032183 (2012). https://doi.org/10.1063/1.4756995

42. M.V. Kovalenko, L. Protesescu, M.I. Bodnarchuk, Properties and potential optoelectronic applications of lead halide perovskite nanocrystals. Science **358**, 745–750 (2017). https://doi.org/10.1126/science.aam7093

43. S. Xu, A. Libanori, G. Luo, J. Chen, Engineering bandgap of CsPbI$_3$ over 1.7 eV with enhanced stability and transport properties. Iscience **24**, 102235 (2021). https://doi.org/10.1016/j.isci.2021.102235

44. G.A. Crosby, J.N. Demas, Measurement of photoluminescence quantum yields. Review. J. Phys. Chem. **75**, 991–1024 (1971). https://doi.org/10.1021/j100678a001

45. D. Magde, R. Wong, P.G. Seybold, Fluorescence quantum yields and their relation to lifetimes of rhodamine 6G and fluorescein in nine solvents: Improved absolute standards for quantum yields. Photochem. Photobiol. **75**, 327–334 (2002). https://doi.org/10.1562/0031-8655(2002)075%3c0327:FQYATR%3e2.0.CO;2

46. Y. Wei, Z. Cheng, J. Lin, An overview on enhancing the stability of lead halide perovskite quantum dots and their applications in phosphor-converted LEDs. Chem. Soc. Rev. **48**, 310–350 (2019). https://doi.org/10.1039/C8CS00740C

47. M. Pols, J.M. Vicent-Luna, I. Filot, A.C. van Duin, S. Tao, Atomistic insights into the degradation of halide perovskites: a reactive force field molecular dynamics study. J. Phys. Chem. Lett. **12**, 5519–5525 (2021). https://doi.org/10.1021/acs.jpclett.1c01192

48. S. Chatterjee, I. Dutta, Y. Lum, Z. Lai, K.-W. Huang, Enabling storage and utilization of low-carbon electricity: power to formic acid. Energy Environ. Sci. **14**, 1194–1246 (2021). https://doi.org/10.1039/D0EE03011B

49. J.E. Pander, J.W.J. Lum, B.S. Yeo, The importance of morphology on the activity of lead cathodes for the reduction of carbon dioxide to formate. J. Mater. Chem. A **7**, 4093–4101 (2019). https://doi.org/10.1039/C8TA10752A

50. B. Kumar, V. Atla, J.P. Brian, S. Kumari, T.Q. Nguyen et al., Reduced SnO$_2$ porous nanowires with a high density of grain boundaries as catalysts for efficient electrochemical CO$_2$-into-HCOOH conversion. Angew. Chem. Int. Ed. **56**, 3645–3649 (2017). https://doi.org/10.1002/anie.201612194

51. Y. Yang, J.P. Robbins, L. Ezeonu, Y. Ma, N. Sparta et al., Probing lattice vibrations of stabilized CsPbI$_3$ polymorphs via low-frequency Raman spectroscopy. J. Mater. Chem. C **8**, 8896–8903 (2020). https://doi.org/10.1039/D0TC02123G